

1 **MultIscale MultiObjective Systems Analysis (MIMOSA): an advanced metabolic modeling
2 **framework for complex systems****

3
4 Joseph J. Gardner¹, Bri-Mathias S. Hodge^{1,2,3}, Nanette R. Boyle^{1,*}

5
6 ¹Chemical & Biological Engineering, Colorado School of Mines, 1613 Illinois St. Golden, CO
7 80403; ²National Renewable Energy Laboratory, 15013 Denver West Parkway, Golden, CO
8 80401; ³Electrical, Computer and Energy Engineering, 425 UCB, University of Colorado,
9 Boulder, CO 80309

10 *Corresponding Author

11
12 **ABSTRACT**

13 In natural environments, cells live in complex communities and experience a high degree of
14 heterogeneity internally and in the environment. Unfortunately, most of the metabolic modeling
15 approaches that are currently used assume ideal conditions and that each cell is identical, limiting
16 their application to pure cultures in well-mixed vessels. Here we describe our development of
17 MultIscale MultiObjective Systems Analysis (MIMOSA), a metabolic modeling approach that can
18 track individual cells in both space and time, track the diffusion of nutrients and light and the
19 interaction of cells with each other and the environment. As a proof-of concept study, we used
20 MIMOSA to model the growth of *Trichodesmium erythraeum*, a filamentous diazotrophic
21 cyanobacterium which has cells with two distinct metabolic modes. The use of MIMOSA
22 significantly improves our ability to predictively model metabolic changes and phenotype in more
23 complex cell cultures.

24 **KEYWORDS**

25 systems biology, agent-based modeling, metabolic flux, multi-paradigm, advanced metabolic
26 model

27 **BACKGROUND**

28 Microbes live in complex communities where they must interact with other organisms and compete
29 for resources to thrive. By leveraging the capabilities of each individual in the community,
30 consortia can achieve outcomes that are not possible by any one individual species. Metabolic
31 engineers are learning from nature and are engineering synthetic consortia to take advantage of
32 endogenous capabilities of specialists to achieve higher yields than pure cultures. One tool that has
33 been used extensively to aide in the rational design of strains are metabolic models (11). The most
34 widely used stoichiometric metabolic models are constraint-based linear programming models
35 which vary in complexity from the relatively simple flux balance analysis (FBA) to more complex
36 FBA models which integrate regulatory and/or thermodynamic constraints (12, 13) or time-
37 dependent responses (14). The wide use of these models is due to the ease of constructing them;
38 access to the genome sequence is enough to build a draft metabolic network. The simplicity of this
39 technique does come at a cost: typical model formulations are limited to modeling steady-state
40 growth of axenic cultures assuming homogenous environmental conditions; while this works for
41 traditional metabolic engineering efforts on single species, it cannot accurately predict the behavior
42 of consortia. There have been a few attempts to expand the applicability of these models to
43 communities (3, 14, 15), but these models require assumptions that oversimplify the system, such
44 as no diffusional limitations and identical or static growth rates for the different organisms. The
45 current benchmarks for constraints-based metabolic modeling of microbial consortia are OptCom
46 (16) and d-OptCom (17) (OptCom's dynamic version). These approaches use inner and outer

47 linear optimization problems to satisfy species and community level objectives, leveraging the
48 inner solution as a constraint for the outer problem. However, this approach still relies on *a priori*
49 determination of relative objective preference as well as predetermination of both species-level
50 and community-level objectives. Additionally, cells are treated as homogenous spatial groups (13)
51 or homogenous species groups (14), which limits the accurate simulation of cells acting
52 individually, interacting with their environment, and ultimately forming communities. These
53 approaches thus discount the complexity of individual cells forming communities and, instead of
54 acting uniformly with neighbors or species, create dynamic intercellular and inter-environmental
55 reactions (13, 18-20).

56

57 To more accurately model the complexity of community growth, a new modeling approach must
58 be developed. We have developed Multiscale MultiObjective Systems Analysis (MIMOSA), an
59 advanced metabolic modeling framework for complex systems. This approach uses a multi-scale
60 multi-paradigm metabolic modeling approach can leverage simple, powerful stoichiometric
61 metabolic models and integrate spatio-temporal tracking of cells, nutrient diffusion, cell-cell
62 interactions and cell-environmental interactions. This approach requires the use of both continuous
63 and discrete variables as well as several different mathematical formalisms to reflect the multilevel
64 behavior in populations. Therefore, we use an agent-based modeling (ABM) framework to allow
65 direct interaction of different levels through the encapsulation of physiological, environmental,
66 and metabolic models. ABM is a bottom-up modeling approach; the model is made up of a set of
67 agents, which are allowed to act independently as long as they follow distinct rules of behavior
68 defined by the user, this allows us to simulate emergent behavior of complex communities that
69 arise from individual agent behaviors (21-24). The system behavior emerges as a result of the

70 many (tens, hundreds, thousands, millions) individuals, each following their own behavior rules,
71 living in a defined environment, interacting with each other and the environment (22). The
72 integration of multiple modeling formalisms to represent disparate sub-systems is a trend common
73 in engineering and science domains (25-29) and has recently seen some developments in the
74 systems biology area (5, 30). Agent-based modeling has been previously applied to both
75 intercellular (12, 31) and multi-cellular processes (32, 33) but has not previously been used to
76 model metabolic fluxes. This multi-scale multi-paradigm approach represents a novel method of
77 integrating individuals (through agents) with previously leveraged dFBA formulations (34, 35),
78 thereby discretizing and separating variables for computational efficient solutions with low *a*
79 *priori* knowledge.

80

81 As a proof-of-concept study, we chose to model *Trichodesmium erythraeum*, a filamentous
82 diazotrophic cyanobacterium. *T. erythraeum* is a major contributor to the global nitrogen cycle; it
83 is responsible for fixing an estimated 42% of all marine biological nitrogen (36) and it leaks 20-
84 50% of the nitrogen it fixes (37), providing surrounding organisms with a biologically available
85 nitrogen source. Unlike other diazotrophs, which either spatially or temporally separate the oxygen
86 sensitive nitrogenase enzyme from the water splitting reaction of photosynthesis (oxygen
87 production), *T. erythraeum* is unique because it simultaneously carries out nitrogen and carbon
88 fixation during the day in different cells along the same filament (trichome). Therefore, it is the
89 ideal model system for the development of MIMOSA: it has structurally identical cells that operate
90 in two distinct metabolic modes (photoautotrophic and diazotrophic), a published genome scale
91 model (3), transcriptome data, and a plethora of *in situ* and laboratory data to both train the model
92 and validate predictions. We use this organism as a test-case for the modeling framework and

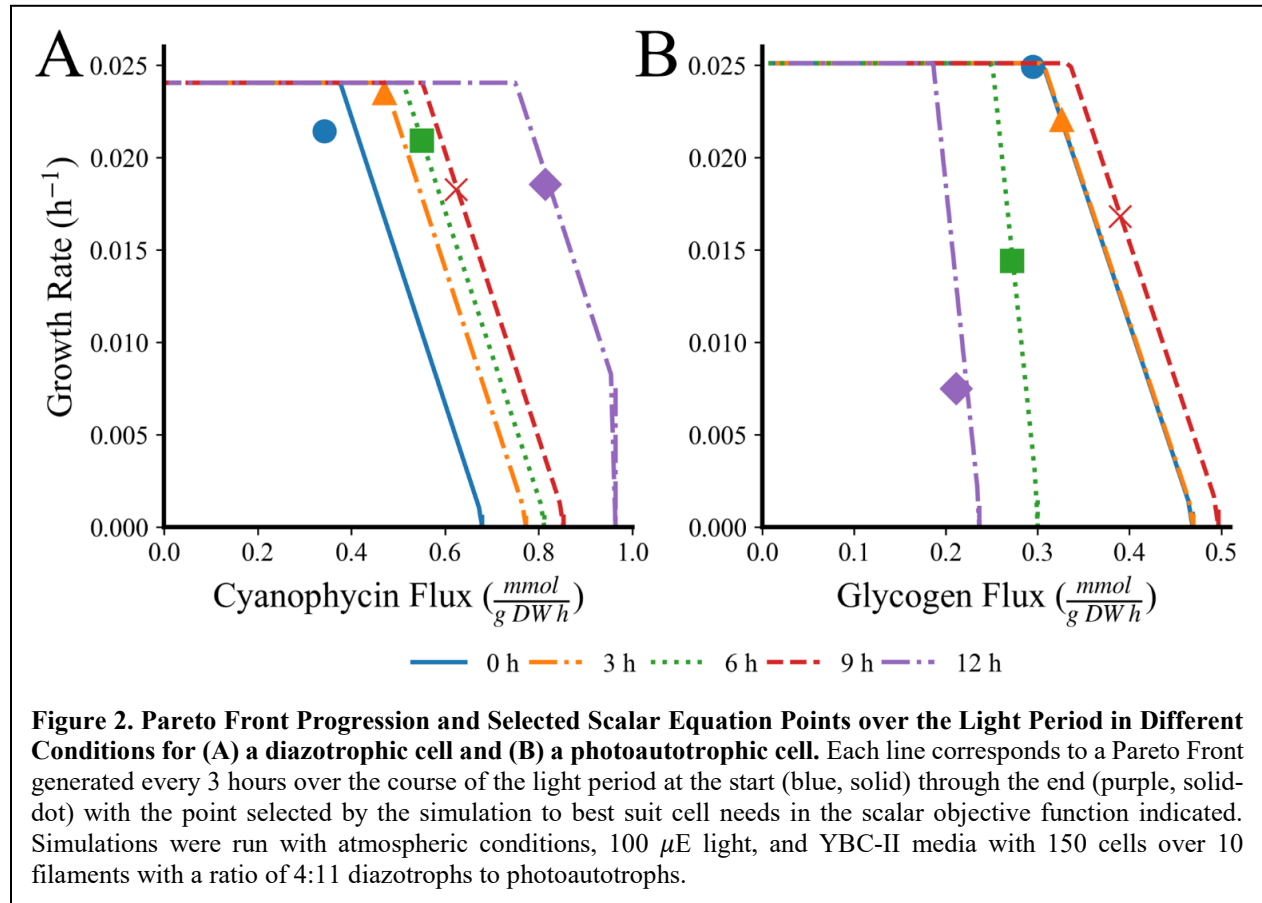
96 **RESULTS**

97 **Model Formulation.** We developed MIMOSA by integrating an updated version of the genome-
98 scale metabolic model (3) (Table S1 for updated reactions) with nutrient diffusion, light diffusion,
99 cell/cell interaction and cell/environment interactions (see Figure 1) using an agent based modeling
100 framework. We have also implemented the use of multiobjective optimization to account for the
101 dual cellular objective of producing biomass and the metabolite which is transacted between cells
102 (glycogen or β -aspartyl arginine, depending on cell type). Constraints were imposed on the model
103 as reported previously (3) with two notable exceptions. First, the ultimate product of nitrogen
104 fixation was changed from ammonium to β -aspartyl arginine, which is the monomer used to create
105 cyanophycin, a nitrogen storage polymer in *T. erythraeum* and other diazotrophic cyanobacteria
106 (38-40). Second, the two major storage polymers, glycogen (modeled as maltose, or two linked
107 glucoses) and cyanophycin (modeled as β -aspartyl arginine), were decoupled from the biomass
108 formation equation so that they could freely accumulate or be metabolized. More detail about the
109 formulation of the model is provided in Methods and Supplemental Text.

110

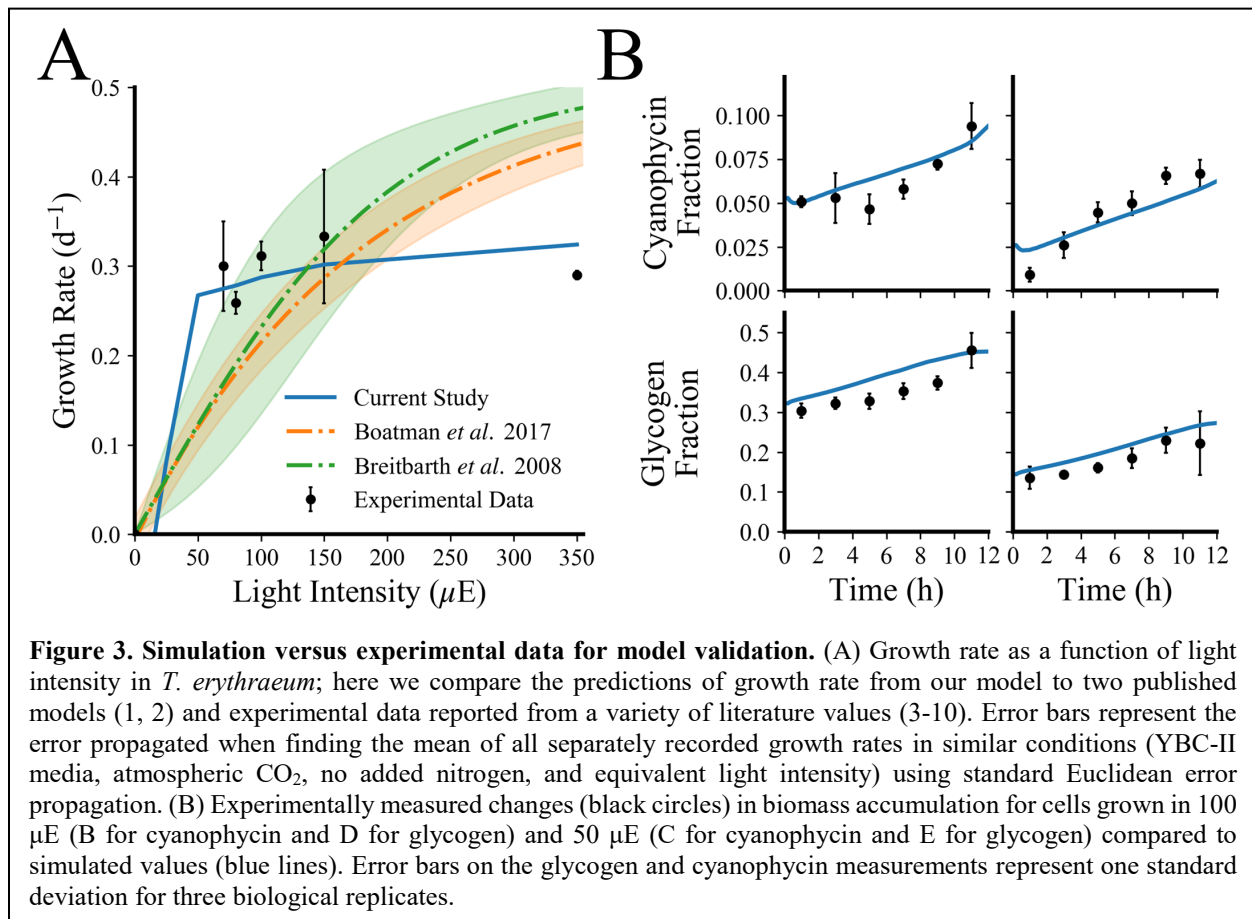
111 **Tracking Changing Cellular Objectives.** MIMOSA evaluates the cellular objective for each cell
112 for each time step based on the changing environmental conditions. As an example of this, we
113 have tracked how the Pareto front changes for both photoautotrophic and diazotrophic cells over
114 time (Figure 2). With increasing time, diazotrophs shift their objective away from biomass toward
115 the production of cyanophycin as carbon becomes more available (Figure 2A). In contrast,
116 photoautotrophic cells see a maximum production of glycogen at 9 hours after the onset of light
117 and then their productivity decreases (Figure 2B). It is notable that every cell in the population is
118 performing these decisions in parallel and Figure 2 is for a single representative cell of each cell

119 type. Cell optimization changed based on environmental conditions and agent rules and the Pareto
120 Fronts representing this behavior in these contexts is visualized in Fig. S1.
121



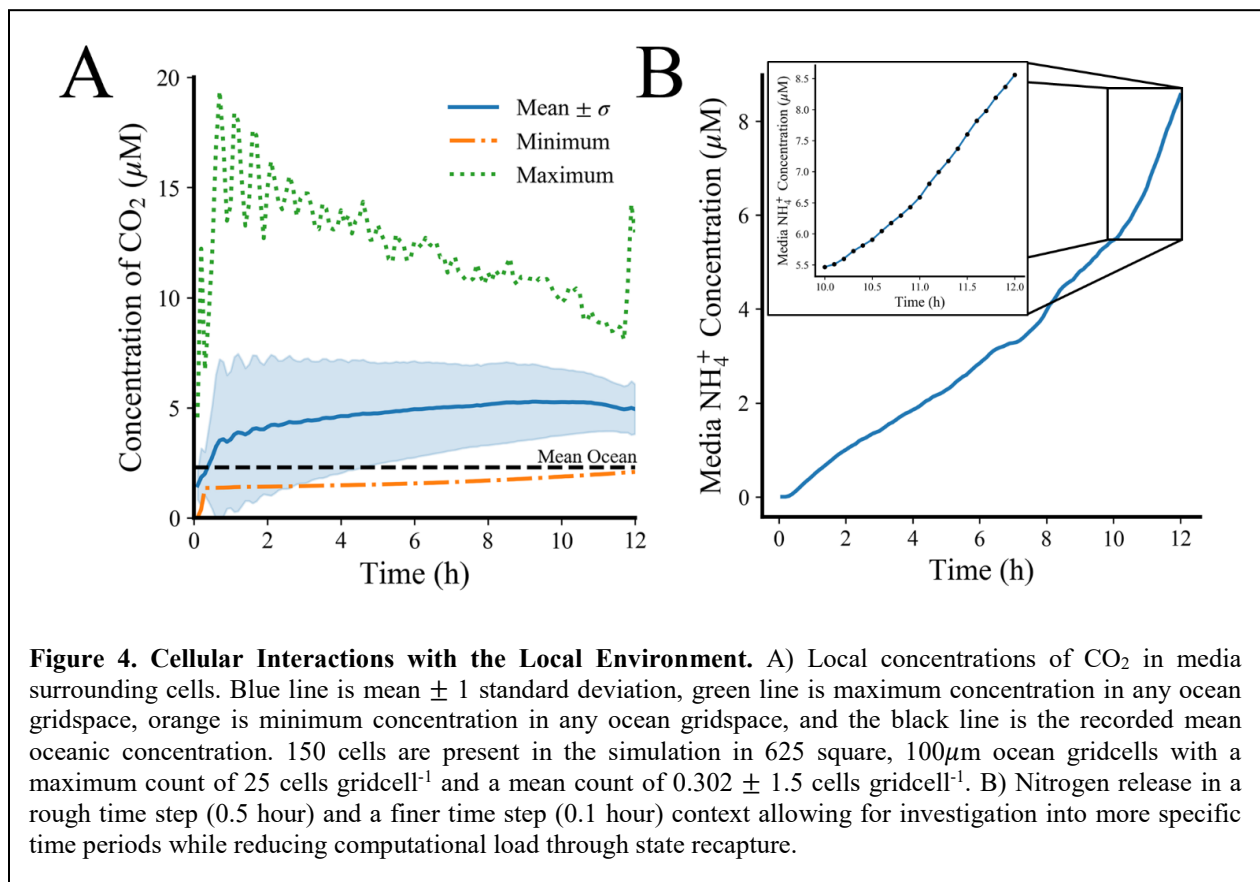
122
123 **Model Validation.** In order to test the predictive accuracy of the model, we predicted growth rate
124 for a variety of different light intensities (Figure 3A) and compared to other published models for
125 *T. erythraeum* (1, 2) as well as other experimentally measured growth rates (1, 3, 6, 9, 10, 41)
126 exhibiting light saturation at higher light intensities. Ultimately, our model is a metabolic model,
127 so it is important that it can also capture the metabolic changes that occur in response to changes
128 in the environment. Therefore, we compared predictions of biomass changes to data collected in
129 our laboratory for growth in different light intensities (see Figure 3B). The model was trained on

130 data collected in 100 μE light and was validated with data collect in 50 μE light over a twelve-
131 hour light period.



132
133 **Cells Alter Their Microenvironment.** An advantage of the modeling approach we have
134 developed is that we can track nutrients in the environment. Carbon dioxide (CO₂) is typically the
135 limiting substrate in aquatic photosynthetic growth due to low ambient concentrations and low
136 solubility; for ambient CO₂, Henry's law defines an equilibrium concentration of 2.3 μM in the
137 ocean. It is well known that photosynthetic microorganisms use carbon concentrating mechanisms
138 (CCM) to concentrate CO₂ near the carbon fixing enzyme, ribulose-1,5- biphosphate
139 carboxylase/oxygenase (RuBisCO) to overcome low selectivity (42); our simulations imply that
140 cells also increase the local concentration of CO₂ immediately surrounding the cell (Figure 4A)

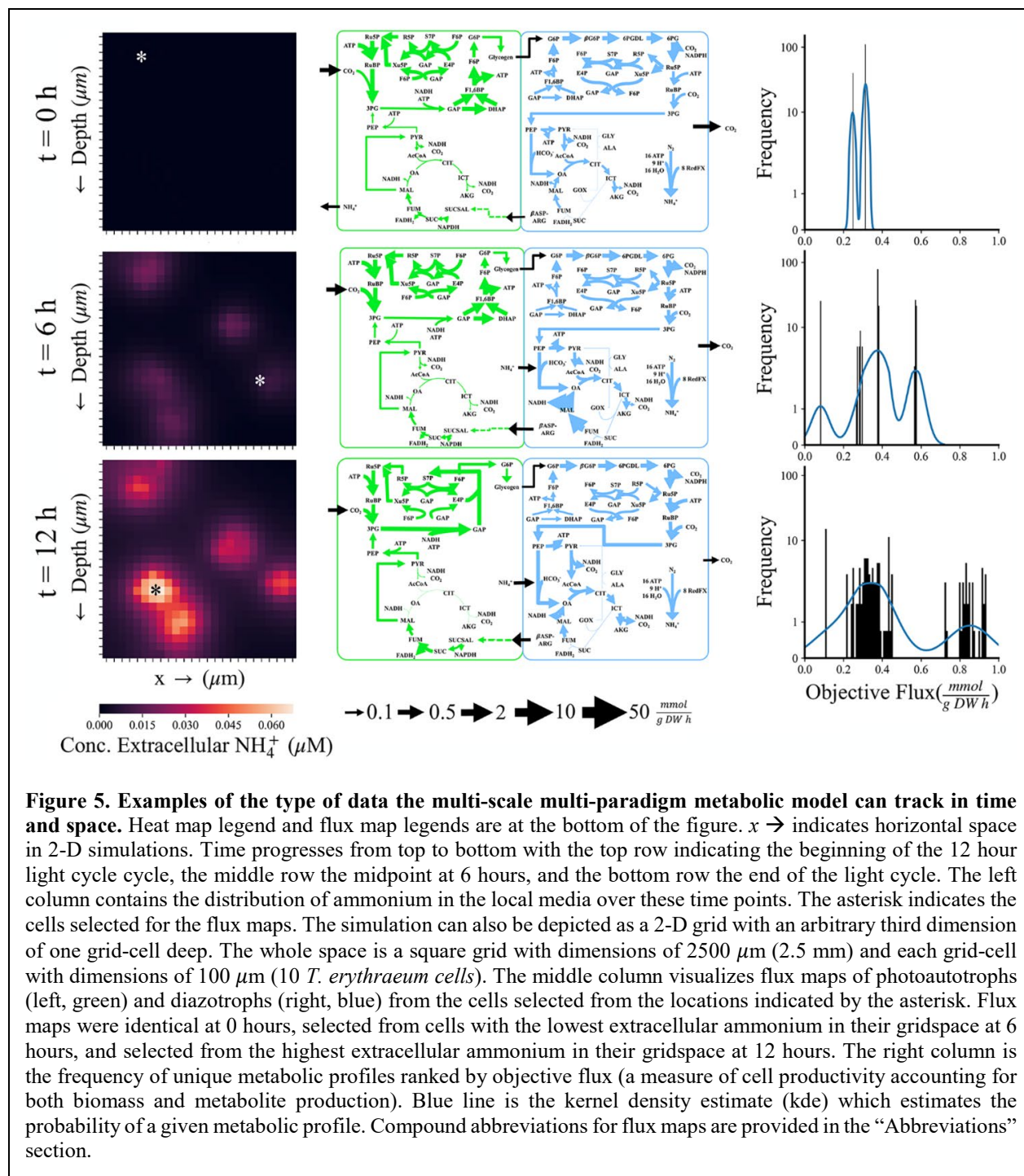
141 and the release of nitrogen to the media including at more frequent time steps (Figure 4B). The
142 simulation covers 150 cells and 10 filaments in a model 0.625 mm^3 environment, corresponding
143 to a filament density of $16 \times 10^6 \text{ trichomes m}^{-3}$, well within the *in situ* ranges of free trichome
144 density (43). This illustrates that the simulation corresponds well quantitatively to realistic local
145 environments. At the end of our simulation, the cells on average can create a microenvironment
146 that is roughly 2 fold higher in CO_2 than the surrounding ocean. By looking at flux through major
147 pathways, it appears that the CO_2 is derived from high fluxes through the oxidative PPP and TCA
148 Cycle in diazotrophic cells (Figure 5).



149
150 **Modeling a Heterogeneous Cell Population.** One of the main advantages of this new modeling
151 approach is that individual cells can be tracked in space and time so the heterogeneity of the
152 population can be quantified (in terms of metabolic flux distributions). As an example, we tracked

153 150 cells over a 12-hour time period with time steps of 6 seconds which results in a total of 18,000
154 metabolic flux maps. Since this is an overwhelming amount of data to visualize, we have chosen
155 to focus on a few representative flux maps (see Figure 5). In the left column, we track how the
156 ammonium composition of the environment surrounding the cells changes with time from the
157 initial seeding of cells at 0 hours to the middle of the daytime period (6 hours) to right before the
158 onset of night (12 hours). These panels depict the release of ammonium into the environment as
159 time progresses, and it is higher in areas where the cell density is highest. This agrees well with *in*
160 *situ* data which reports that *T. erythraeum* leaks 30-50% of the nitrogen it fixes (37); our
161 simulations predict that approximately 20% of the nitrogen fixed by the community is excreted
162 into the medium. It is also important to note that the majority of ammonium is released by the cells
163 in the second half of the day; during the first 6 hours, the cells release a total of 1.28 μ moles
164 compared to 4.61 μ moles in the last six hours of the day. Again, this agrees with previous literature
165 reports that the rate of nitrogen fixation peaks at midday (44), therefore we would expect more
166 secretion of ammonium after peak nitrogenase activity. Select flux maps of cells growing in areas
167 of low ammonium (top), medium ammonium (middle) and high ammonium (bottom) are depicted
168 in the middle column of Figure 5. At the beginning of the simulations, cells are seeded in an
169 environment that is identical to the defined marine medium YBC-II and because of this, they have
170 identical flux maps as shown by the distribution graph in the right column. At time 0, we have a
171 bimodal distribution because there are two cell types: photoautotrophic and diazotrophic.
172 Photoautotrophic cells have high flux through the Calvin Cycle and the diazotrophic cells are
173 operating in a more respiratory mode, with high flux through both the oxidative PPP and TCA
174 Cycle. As the cells grow and start to experience more heterogeneity in their environment, they
175 respond by differentiating their metabolism within the filament (Figure S2). First, this is evident

176 in the frequency distribution plot, where they are both diverging in terms of total metabolic flux
177 distributions and moving toward achieving optimal flux in terms of the objective function for both
178 $t = 6$ hours and $t = 12$ hours. By comparing the changes that occurs in metabolic flux between areas
179 of low, medium, and high ammonium, we can learn a few things about cellular physiology. In all
180 cases, photoautotrophic cells have high flux through the Calvin cycle and an incomplete TCA
181 Cycle, which has been widely reported in cyanobacteria grown phototrophically (45). In the case
182 of *T. erythraeum*, succinic semialdehyde is derived from the nitrogen storage compound
183 cyanophycin and is fed into the TCA Cycle to support the production of biomass precursors and
184 glycogen (through gluconeogenesis). When external ammonium is high, photoautotrophic cells
185 have less flux to glycogen, presumably because they do not need to provide as much to the
186 diazotrophic cells to obtain fixed nitrogen in return. Investigations into imbalances in both
187 metabolites and relative cell quantity display mechanisms of ammonium loss to the environment.
188 Figure S3A illustrates how a lack of glycogen flux results in a higher loss of ammonium (with the
189 exceptions of recently divided cells which metabolize glycogen with high ammonium loss) while
190 Figure S3B visualizes a clear minimum ammonium release in the recorded range of percent
191 diazotrophs per filament (between 15 and 30%). Diazotrophic cells have high flux through both
192 the oxidative PPP and the TCA cycle which still utilizing carbon fixation reactions such as
193 RuBisCO and PEP carboxylase and carbon conserving reactions like the glyoxylate shunt. Flux
194 through the glyoxylate shunt increases as the availability of ammonium increases outside the cell,
195 which is likely in response to the lower glycogen transfer from the photoautotrophs.



196

197 **Elucidating Rules of Cell Physiology.** A key feature of agent-based modeling is the ability to

198 model emergent behaviors in populations. We do not know all the rules of behaviors that define

199 *T. erythraeum* a priori but by comparing simulations to observed *in situ* data and iterative

200 improvement of the model, some rules can be elucidated. One trait that is widely variable in nature
201 is filament length. It has been widely accepted that the average filament length is 100 cells (46)
202 but more recent studies have suggested that they are typically much shorter, with a geometric mean
203 of 13.2 ± 2.3 cells per filament, but with a mean range of 1.2 to 685 cells per filament *in situ* (47).
204 Conditions for *in situ* sampling are widely variable so we hypothesized that filament length plays
205 a role in maintaining growth in different environments: low light, low CO₂ and low N₂. We used
206 the model to investigate which conditions might favor shorter or longer filaments (Figure 6). For
207 each simulation, 150 total cells were seeded but in different trichome lengths (10, 30, 75, and 150
208 cells/filament) with and a ratio of diazotrophs to photoautotrophs of 3:7. In terms of growth rate,
209 across all conditions we tested the shorter filaments had faster growth. This implies that diffusional
210 limitations of nutrients into the cell and metabolites within the filament between different cell types
211 start to hamper growth rate at longer filament lengths. The relative decline in growth rate is less
212 dramatic for 25 μ E when comparing across filament length, but when compared to other light
213 conditions, there is a dramatic drop in growth rate for shorter filaments at low light. This indicates
214 that longer filaments are capable of compensating for less light better than shorter filaments,
215 perhaps due to increased surface area. Next, we examined the effect of filament length on
216 cyanophycin composition for the same growth conditions as above. In every condition except low
217 nitrogen, filaments with 75 cells appear to have more cells with above average cyanophycin
218 content than other filaments lengths. Smaller nitrogen compounds (NH₄⁺, amino acids, urea, etc.)
219 can theoretically be used to support growth, permitting cyanophycin to be a longer-term storage
220 compound. This is a possible explanation for the increase of cyanophycin in longer filaments. As
221 filaments are longer, diffusive limitations become more pronounced, meaning that nitrogen
222 gradients will remain in nitrogen replete cells longer and will be remade into cyanophycin as

223 opposed to being metabolized for growth. This makes intuitive sense: not only is there a final drop-
 224 off at 150 cells, the distribution of cyanophycin content within the cells becomes larger, suggesting
 225 that some cells are starved for nitrogen and some are nitrogen replete. It is probable that filaments
 226 have adapted to leverage diffusion to both sequester nitrogen and to mitigate futile cycling of
 227 carbon and nitrogen compounds when diatomic nitrogen is available. The pattern of cyanophycin
 228 content diverges for cells in nitrogen limited environments due to overall shortages of nitrogen
 229 within the filament.

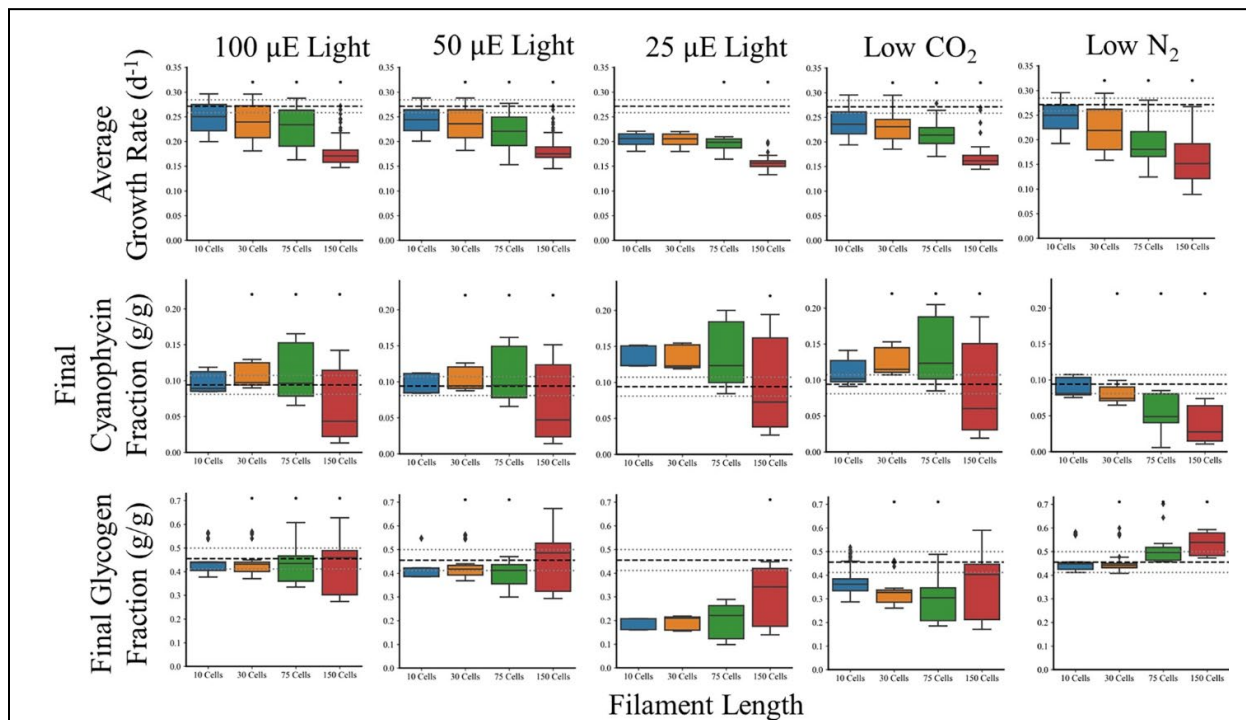


Figure 6. Trichome length affects the performance of the community. Trichomes were varied in initial length from short (10 cells filament⁻¹) to long (150 cells filament⁻¹) but with identical diazotroph: photoautotroph ratios of 3:7 (excepting 75 cells filament⁻¹ which was 3.1:7) and initial cell counts (150 total) in the total population. Black asterisks are Student's T-tests P-Values < 0.05 when comparing that cellular population to the 100 μE case in every group. Dashed black lines are experimentally measured values and the gray dashed lines are their standard errors measured in the Boyle Laboratory (0.271 ± 0.0129 d⁻¹ for growth rate, 0.0939 ± 0.0131 g cyanophycin/g DW, 0.455 ± 0.0440 g glycogen/g DW). Growth conditions represent the columns progressing as follows: 100 μE light in YBC-II media and atmospheric conditions, 50 μE light in YBC-II media and atmospheric conditions, 25 μE light in YBC-II media and atmospheric conditions, 1.25 mM (versus 2.5 mM) HCO₃⁻ and 200 ppm (versus 400 ppm) CO₂ in otherwise atmospheric conditions and YBC-II media with 100 μE light, and 0.395 atm (versus 0.79 atm) N₂ in otherwise atmospheric conditions and YBC-II media with 100 μE.

230

231 Finally, we investigated how glycogen content of cells changes due to filament length. The first
232 pattern to note is that as length increases, the heterogeneity of the filament in terms of glycogen
233 content also increases. This illustrates the importance of tracking individual cells because they are
234 experiencing different environments and responding in different ways. Longer filaments also
235 appear to be able to maintain glycogen content more readily than shorter filaments in all stress
236 conditions we tested. Finally, nitrogen limited growth results in increased glycogen content as seen
237 in other cyanobacteria (48). It appears that longer filaments in N limited growth can accumulate
238 more carbon, perhaps again due to higher surface area and hence more energy from light
239 harvesting. Our simulations agree well with published studies; it has been reported that growth
240 rate and light intensity are both inversely correlated to filament length (49). This data indicates
241 that filament length is largely determined by external cues rather than genetically.

242

243 **DISCUSSION**

244 MIMOSA enables the most detailed and accurate metabolic modeling of complex systems to date
245 by allowing coupling of several different mathematical formalisms describing natural phenomena,
246 behavioral rules, and metabolism into a multi-scale multi-paradigm model. In constructing
247 MIMOSA, we have added several features to enable us to more accurately predict phenotypes. A
248 key feature of MIMOSA is the use of a multi-objective optimization approach. Unlike fast growing
249 bacteria, which have successfully been modeled using a single objective function of maximum
250 biomass (50), slow growing organisms have more complex objectives. In our simulations, *T.*
251 *erythraeum* cells must achieve a delicate balance between biomass formation and the production
252 of either glycogen or cyanophycin due to the symbiotic relationship between two cell types in the
253 same filament. Photoautotrophs cannot function optimally without a biologically available form

254 of nitrogen from the diazotrophs and the diazotrophs cannot support their metabolism without
255 reduced carbon from the photoautotrophic cells. The use of multi-objective optimization allows us
256 to describe this trade-off more accurately and by calculating the Pareto Front *a priori* we can also
257 reduce computational effort. We have also accounted for changes in biomass composition that
258 occur in response to changes in the environment or as a result of building carbon and nitrogen
259 reserves during the day by decoupling the biomass equation. This allows the model to respond
260 more fluidly to changes in the environment, which more closely mimics what cells experience in
261 nature; for example, macro- and micro-nutrient stresses have been well known to cause changes
262 in metabolism such as lipid and carbon accumulation (51-56). As such, the inclusion of metabolite
263 and nutrient diffusion to augment metabolic optimization is a critical aspect of the model.

264

265 The influences of nutrient and energy availability in conjunction with population characteristics
266 were studied to determine community and cellular adaptations to environmental perturbations. The
267 model allows us to quantify the changes in the microenvironment around the cell compared to the
268 bulk properties of the environment (Figure 4A) as well as to see how these changes affect the
269 distribution of carbon and nitrogen inside the cell (Figure 5). These can be supplemented with
270 “zooming in” on specific time steps to enhance investigation to rapidly occurring phenomena
271 (Figure 4B). Not only did our predicted growth rates quantitatively match the experimental data,
272 it was better able to capture effect of light saturation on growth rate; light intensities above 100 μE
273 have little to no effect on growth rate (2, 49, 57-59). Our simulations agree well with the
274 experimental data, however, there are differences that can be explained by the differences between
275 our experimental conditions and our simulations. The main difference being the effect of diurnal
276 light; *T. erythraeum* will not grow without diurnal day/night patterns, therefore the experimental

277 data was collected from cells that were grown in 12 h: 12 h day/night cycles but the model is for a
278 single 12-hour day time period. The addition of diurnal light patterns in future iterations of this
279 model will help to improve the light dependent growth phenotype. Even so, the model is able to
280 visualize community coordination and development during the 12 hour light period, exhibiting the
281 increased release of ammonium to the media in the afternoon, consistent with the observation that
282 nitrogenase activity peaks midday (44). Moreover, the individualized resolution of metabolic
283 optimization can probe the nuances of intercellular, intracellular, and cell-environment
284 interactions. Analysis of metabolic flux reveals a spontaneous partial/linear TCA Cycle in
285 photoautotrophic cells consistent with previous reports (45). Cells also naturally coordinate to
286 provide glycogen and cyanophycin transfer between cells, yielding oxidative behavior in
287 diazotrophic cells through glycolysis with the possible side effect of oxygen consumption as a
288 mechanism to protect nitrogenase as suggested in experimentation (58). Meanwhile,
289 photoautotrophs naturally perform reductive carbon fixation coupled with utilization of the lower
290 TCA Cycle to degrade arginine. These metabolic functions are affected by extracellular forces
291 which are integrated into this model. For example, high ammonium environments result in
292 declining gluconeogenesis in photoautotrophs (12 hours in Figure 5), likely since these cells are
293 energetically limited and use cyanophycin as an energy source instead of light. Diazotrophs are
294 prone to these environmental cues as well as low ammonium environments enhance light TCA
295 Cycle to enhance recycling of amino acid byproducts from a lack of nitrogen. These observations,
296 coupled with the diversity of metabolic profiles available to a relatively small population, By
297 integrating modeling of other phenomenon with constraints based metabolic models, we were able
298 to simulate *T. erythraeum* cultures that more accurately represent both *in situ* and laboratory data.
299

300 One of the many advantages of using this multi-paradigm framework is that we can simulate
301 emergent behavior of a population. *In situ* data reports a wide mean range of trichome length from
302 1.2 to 685 cells (47); we used the model to investigate possible causes because this is a difficult
303 phenotype to investigate experimentally. Our simulations suggest that even though longer
304 filaments suffer from diffusional effects that limit growth, they are better able to handle stress
305 (Figure 6) consistent with literature. Increased surface area in longer filaments minimizes the effect
306 of lower light because the filament can harvest more light per volume. Also, the larger filaments
307 are better able to maintain the average composition of storage compounds despite low carbon or
308 low nitrogen conditions. Therefore, we would expect in areas of nutrient or light stress, the filament
309 length would be longer.

310

311 One of the other unusual phenotypes of *Trichodesmium* that we were able to investigate using
312 MIMOSA was leaking 30-50% of the nitrogen it fixes. Nitrogen fixation is an incredibly energy
313 intensive process, costing the cell 8 ATP per ammonium, so it is not clear why *T. erythraeum*
314 would excrete 30 – 50%. Despite using optimization to solve for fluxes, which should minimize
315 energy losses, our simulations predict approximately 20% of the fixed nitrogen is excreted into the
316 medium (Figure S4) which implies that this is a metabolically driven phenomenon. Further
317 investigation has led us to develop three hypotheses on why this occurs: carbon limitation in
318 diazotrophs, energy limitation in photoautotrophs, and imbalances between photoautotroph:
319 diazotroph ratios. In the first case, photoautotrophs are unable to create glycogen chains and
320 instead must start from a higher energy substrate than carbon dioxide (like succinic-semialdehyde)
321 or must perform glycolysis on arginine derivatives to achieve energetic viability (Figure S3A).
322 Second, population imbalances cause nitrogen to be produced faster than it can be anabolized into

323 β -aspartyl-arginine chains and is released into the media, meaning there is an optimal ratio of cell
324 types (Figure S3B). It is also possible that carbon limited diazotrophs are unable to manufacture
325 full β -aspartyl-arginine chains and proton imbalances require ammonium release to the medium
326 instead of passage to surrounding photoautotrophs.

327

328 MIMOSA enables the tracking of cellular-level environmental changes and the impact that they
329 have on a metabolic model, opening the door to more accurate modeling of multi-cellular systems
330 and the *in silico* investigation of the complex interactions between different cell types within an
331 organism, and different species in a community. This is the first report of a metabolic model that
332 integrates nutrient and light diffusion, cell/cell interactions and cell/environment interactions and
333 we have used it to accurately predict growth, cellular composition and to investigate the unique
334 physiology of *T. erythraeum*, which has filaments of both diazotrophs and photoautotrophs in close
335 proximity. It establishes that this organism can effectively adapt to different conditions at three
336 levels: the genetic level through division of labor in separate cell types, the metabolic level through
337 relatively open-ended metabolic capabilities as well as further division within types, and at the
338 population level to harness diffusional and physical interactions with the environment. MIMOSA
339 is also a readily adaptable modeling framework – the addition of additional species to the model
340 only requires the availability of a genome-scale metabolic and a few rules of behavior to be added.
341 While we focused the proof-of-concept study of *T. erythraeum*, MIMOSA is a modeling
342 framework that can be used to model a variety of more complex systems including applications in
343 ecology, human health and metabolic engineering.

344

345 **MATERIALS/METHODS**

346 **Cell Culture Conditions**

347 Cells were grown as described previously (3). *Trichodesmium erythraeum* IMS101 cells were
348 acquired from the Bigelow Laboratory for Ocean Sciences (East Boothbay, ME, USA). Cells were
349 grown in a New Brunswick (Hamburg, Germany) with 100 and 50 μE in 12h light/12h dark cycles.
350 Cells were grown in artificial seawater YBC-II medium (60) at pH 8.15-8.20. CO_2 was maintained
351 at atmospheric concentration. All chemicals were obtained from Sigma-Aldrich (St. Louis, MO).
352 Growth rate was monitored by measuring chlorophyll absorbance (61) from 50 mL of culture every
353 two days. Cyanophycin and glycogen were measured every four hours from the beginning of the
354 light cycle (9 AM) to its end (9 PM). Total biomass mass was determined by dry weight analysis,
355 cells were filtered with a Whatman 0.22 μm cellulose-nitrate filter and dried overnight at 100°C.

356 **Biomass Quantification**

357 Carbohydrates were measured colorimetrically using the anthrone method (62) against glycogen
358 as a standard. Cyanophycin was extracted by disrupting 740 μL of 250 mL cells concentrated to 2
359 mL via filtration and rinsing with TE buffer with 2.70 mg/mL lysozyme overnight at 37 °C,
360 centrifuging at 16,100 x G for 5 min, and resuspending the pellet in 1 mL of 0.1 M HCl (in which
361 cyanophycin is soluble) for 2 h. The extraction was repeated on the pellet, the supernatant fractions
362 were combined, and cyanophycin was quantified colorimetrically using the Sakaguchi reaction
363 (63).

364 **Mass Balance Constraints.** Constraints based metabolic models are based on mass balances,
365 therefore it is imperative that we develop accurate accounting of each element. Therefore, we used
366 training data (Table S2) to estimate normal cellular consumption (Table S3). Average objective
367 fluxes were estimated using mass balances around biomass and metabolite production with the
368 formulation:

369

$$U = M + G + P + L \quad (1)$$

370 Where U corresponds to uptake, M is the nitrogen or carbon required for maintenance metabolism,
371 G is the accumulation of fixed carbon or nitrogen during growth into non-biomass metabolites, P
372 is the accumulation of fixed carbon or nitrogen that is passed to the other cells, and L is the carbon
373 or nitrogen leaked into the surrounding media. This can be further detailed into carbon and nitrogen
374 energy balances (defined as above with the subscript “N” for nitrogen and “C” for carbon):

$$U_N = 2\nu_{N_2} + \nu_{NO_3^-} + \nu_{NO_2^-} + 2\nu_{urea} \quad (2)$$

$$M_N = -5 \frac{\Delta m_{c_{ph}, Night}}{N_{c_{ph}} \bar{X}_t \Delta t} \quad (3)$$

$$G_N = \mu Y_{N/X} \quad (4)$$

$$P_N = 5 \frac{\Delta m_{c_{ph}, Day}}{N_{c_{ph}} \bar{X}_t \Delta t} \quad (5)$$

$$L_N = -\frac{\Delta C_{NH_4^+}}{\bar{X}_t \Delta t} \quad (6)$$

375 Where ν corresponds to flux of the substrate (indicated in the subscript), m is mass, N is molar
376 mass, the subscript c_{ph} is cyanophycin, \bar{X}_t is average biomass over the measured time period (Δt),
377 μ is growth rate, $Y_{N/X}$ is the nitrogen stoichiometry in biomass estimated by the biomass
378 composition. The stoichiometric coefficients represent the number of nitrogen atoms in each
379 molecule; 2 per diatomic nitrogen and 5 per β -aspartyl arginine. The flux of nitrogen (ν_{N_2}) is
380 measured and recorded via the acetylene assay for nitrogenase activity as recorded in the literature
381 for the same growth conditions. G_N was approximated using the model’s prediction for cellular
382 composition of nitrogen using the biomass equation and balanced equations. The fraction of

383 cyanophycin in biomass was measured analytically at 6 timepoints throughout a single 12-hour
384 daytime period (See *Biomass Quantitation* in methods). Ammonium release over a 12-hour period
385 was below detectable limits ($< 1 \mu\text{g/L}$) (64) in our laboratory experiments. If we re-arrange this
386 equation to solve for the average flux of nitrogen into a single cell, \bar{v}_N , we obtain the following
387 equation which can be used to solve for \bar{v}_N or v_{N_2} :

$$\bar{v}_N = 2v_{N_2} + \frac{\Delta C_{NH_4^+}}{\bar{X}_t \Delta t} = \mu Y_{N/X} - 5 \frac{\Delta m_{cph, Night}}{N_{cph} \bar{X}_t \Delta t} + 5 \frac{\Delta m_{cph, Day}}{N_{cph} \bar{X}_t \Delta t} \quad (7)$$

388 Assuming each cell requires the same amount of nitrogen, that only diazotrophs reduce diatomic
389 nitrogen, that the average ratio is 4:1 photoautotrophs to diazotrophs (44) for estimation of training
390 data for consumption and production, and that cells do not release ammonium at optimal
391 production, maximum nitrogen flux into a photoautotrophic cell can be approximated as:

$$\bar{v}_{cph} = \frac{2}{5} v_{N_2} \quad (8)$$

392 The same approach is taken for the carbon mass balance.

$$U = M + G + P \quad (9)$$

393 Where:

$$U_C = v_{CO_2} \quad (10)$$

$$M_C = -12 \frac{\Delta m_{gly, Night}}{N_{gly} \bar{X}_t \Delta t} \quad (11)$$

$$G_C = \mu Y_{C/X} \quad (12)$$

$$P_C = 12 \frac{\Delta m_{gly, Day}}{N_{gly} \bar{X}_t \Delta t} \quad (13)$$

394 And:

$$v_{CO_2} = \mu Y_{C/X} - 12 \frac{\Delta m_{gly, Night}}{N_{gly} \bar{x}_t \Delta t} + 12 \frac{\Delta m_{gly, Day}}{N_{gly} \bar{x}_t \Delta t} \quad (14)$$

395 In this case, the variables are the same except for subscripts C (carbon), gly (glycogen). And CO_2 .
396 G_C represents the stoichiometric predictions of elemental composition and v_{CO_2} is approximated
397 using equation 10. This allows prediction of maximal glycogen flux (assuming 12 carbon
398 molecules per glycogen, since it is modeled as disaccharide glucose or maltose) using:

$$\bar{v}_{gly} = \frac{v_{CO_2}}{12} \quad (15)$$

399 **Development of Agent Based Model.** Repast Simphony (65) in Java was used as the agent-based
400 modeling framework in which differentiated multi-objective metabolic models of *Trichodesmium*
401 *erythraeum* are contained. It contains three agent types – Ocean, Cells, and Filaments. The Cells
402 agent contains two sub-agents representing each cell type: photoautotrophs and diazotrophs and is
403 responsible for intracellular processes and decisions. The Ocean agent defines and calculates the
404 extracellular environment and the Filaments agent organizes the Cells and modulates their
405 transactions.

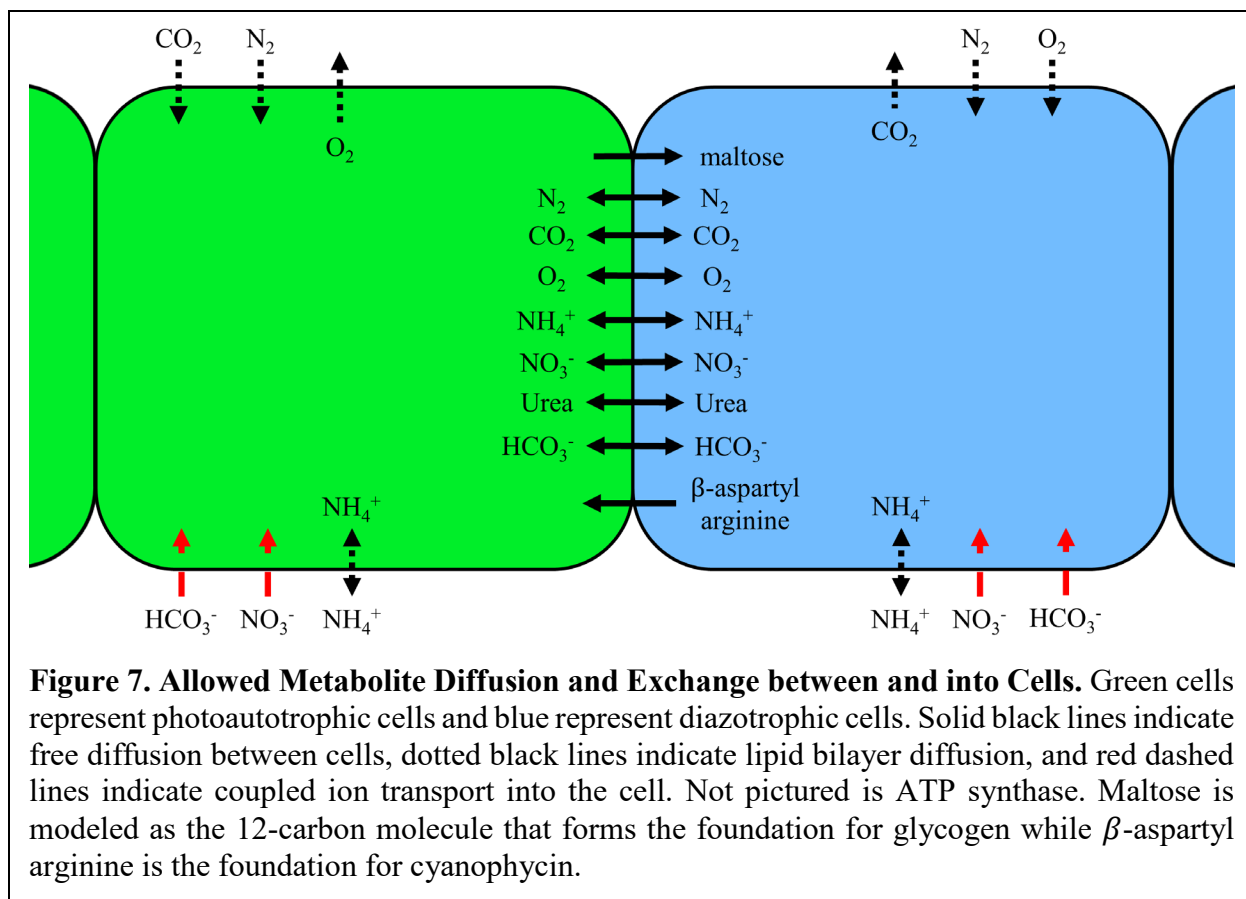
406 *Cells*

407 Cell agents (cells) are generated for each individual cell in the model. These contain two subtypes,
408 photoautotrophs and diazotrophs, but contain several consistent elements between the two.
409 Simulation variables are summarized in Table S4. All cells reproduce according to the same rules:
410 cells divide according to sampling from the weighting distribution described above if that sample
411 is bigger than the cell mean cell, cells only extend from the ends, and cells can only divide into
412 diazotrophs if there is a diazocyte under development (decided at the filament level if the filament
413 is nitrogen limited). When a cell is large enough, it converts to fully stationary growth, producing
414 only metabolites and creating a larger and larger metabolic gradient between cells without *de novo*

415 biomass synthesis. This prevents a cell from becoming excessively large in the center of the
416 filament. Cells will die if they cannot produce the requisite maintenance ATP through metabolism
417 or catabolism.

418

419 Cells allow metabolites to diffuse through the lipid bilayer using permeabilities reported in the
420 literature (Table S5). This mechanism represents a non-zero leakage scenario that was nevertheless
421 much slower than intrafilamental diffusion (Table S6). Scavenging from the environment for
422 compounds which carried no evidence of active transport followed these same rules and was
423 therefore prone to concentration gradients. Active transporters, on the other hand, allowed the cell
424 to uptake whatever concentration of compound was necessary subject to its presence in the local
425 ocean grid. Allowable exchange of metabolites between cells is illustrated in Figure 7. If several
426 cells compete in that grid space, access to the available molecule was divided equally among those
427 cells.



428

429 *Subclasses: Photoautotrophs and Diazotrophs*

430 Both subclasses define the uptake constraints and send to a Python file that decides whether the
431 cell metabolizes or catabolizes based on those constraints using the multi-objective metabolic
432 model previously described (see *Supplemental Information: Routine Metabolic Optimizations*).
433 The cell then updates its internal metabolites based on the optimization results, diffuses
434 metabolites, divides if possible, and uptakes from its local environment. Model bounds are
435 calculated using local concentrations to calculate maximum flux bounds excepting β -aspartyl
436 arginine which is further limited to 8% of available nutrients (See Figure S5). These methods are
437 handled by three ScheduledMethods that Repast Symphony schedules in specific progression.
438 Together with the Ocean Agent's updates, the individual cell actions (as dictated by the metabolic
439 model) form the core of the simulation. A more detailed flow chart for cell decision making can

440 be found in Figure S6. Progression through these steps is identical for cell types, but the metabolic
441 static variables (objectives, gas uptake, etc.) are different between the two subclasses, necessitating
442 separate methods.

443

444 *Ocean*

445 The ocean agent is responsible for tracking cells and modeling external nutrients. Its main task is
446 facilitating diffusion between cells and locations as well as approximating an uptake radius for
447 cells. Each ocean represents a uniform, static, abstract area of the overall grid space with a uniform
448 dimension space of $\delta \times \delta$ where δ is a user defined parameter. This set of simulations was
449 conducted with time steps of 0.1 hours as a moderate value between diffusion phenomena (on the
450 order of seconds along the length of a filament) and doubling time (on the order of 50 hours).
451 Metabolites are assumed to freely diffuse in a dilute seawater environment between cell filaments
452 (Table S6) and assumed to be uniform within the grid, given the relatively long time step compared
453 to the rate of diffusion over such small dimensions. If the impacts of metabolic diffusion limitations
454 were of interest, the time step within the framework could be made appropriately small to more
455 accurately track metabolites, at cost of increased computational burden. Each ocean gridcell
456 diffuses molecules into its adjacent ocean gridcells assuming discretized slab diffusion in two
457 dimensions. This is done using a previously developed discrete algorithm for diffusion in a grid
458 (66):

459

$$\Delta \bar{f}(x_i) = A \sum_{j=1}^n (f(x_i^j) - f(x_i)) e^{-d_j^2/\eta} \quad (16)$$

460

$$d_j = |x_i - x_i^j| \quad (17)$$

461

$$A \sum_{k=1}^n e^{-d_j^2/\eta} = 1 \quad (18)$$

462

463 Where $\Delta \bar{f}(x_i)$ is the change in concentration of metabolite in grid space x_i over a time step, A is
464 the normalization constant to be calculated by solving the third equation within the entire
465 neighborhood to ensure conservation of mass within the neighborhood, d_j is the distance between
466 grid space x_i and its grid neighbor x_i^j and η is the diffusivity control of the system over the time
467 step. As $\eta \rightarrow 0$ diffusion halts and as $\eta \rightarrow \infty$ diffusion becomes instantaneous. In this study, $\eta =$
468 $4\mathcal{D}\Delta t$ as in the original Fick's Law.

469

470 Diffusion is calculated using two steps, one forward and one reversing the order of gridspace
471 calculation, to mitigate the effect of order on estimating the concentration gradient (Figure S7).
472 Excess ammonium is secreted into the environment using a membrane diffusion coefficient. Cells
473 are allowed to uptake any metabolite/nutrient in YBC-II medium; the only extracellular products
474 allowed in simulations are small molecules, such as CO_2 and NH_4^+ which diffuse through the
475 membrane, as well as compounds that have experimental evidence of transporters from proteomic
476 analysis or transcriptomic analysis (estimated using membrane diffusion outwardly and free
477 diffusion for gases or active transporters for ions/molecules inwardly) in Table S7 (67, 68).

478

479 The Ocean Agents also manage diffusion of metabolites from marine sinks and through the gas-
480 liquid surface interface with the atmosphere. This is done assuming equilibrium concentrations of

481 dissolved gases defined by Henry's Law and mono-directional slab diffusion for CO₂, O₂, and N₂.
482 Table S6 lists the free diffusivities of compounds and Table S8 lists the Henry's Constants for
483 atmospheric compounds, and Figure S7 demonstrates the movement of diffusive molecules
484 through the simulation.

485

486 Furthermore, light diffusion to cells is defined as a function of their y coordinate according to the
487 equation:

$$I = I_0 e^{-ky} \quad (19)$$

488 Where I is light intensity, k is the extinction coefficient of light in seawater, and y is the depth
489 below the surface of the individual cell.

490

491 *Filaments*

492 Filament Agents are responsible for organizing cells, managing movement, splitting to promote
493 diazotroph development, and defining cell type after division. Random walk movement (to
494 simulate the lack of control cells have over lateral motion) is simulated by generating a random
495 direction that has an empty grid space for every cell in the filament. Cells move within a user
496 defined interval of time or if their growth is impeded by another filament, in which case growth is
497 halted until the cells move away from each other. The filament forces splitting into two separate
498 filaments when nitrogen is limiting growth and neither filament end is undergoing diazotroph
499 development (meaning that another diazocyte is required). Filament Agents decide the next cell
500 type using this inequality:

501

$$\frac{\sum_i \varepsilon_i^{DZ}}{n_{DZ}} > \frac{\sum_i \varepsilon_i^{PA}}{n_{PA}} \quad (20)$$

502

503 Where ε is the Pareto Efficiency of the given cell type and n is the quantity of that cell type in the
504 filament. The Pareto Efficiency is quantified as the sum of the objective fluxes divided by their
505 Pareto Optimum (from experimental results) divided by the number of objectives.

$$\varepsilon_i^c = \sum_j \frac{v_j}{v_j^{exp}} \quad (21)$$

506 If inequality (20) is satisfied, the cell prioritizes diazotroph development, otherwise it prioritizes
507 photoautotroph development. If a diazotroph region is currently under development, the filament
508 adds another cell to that region. If there is no diazotroph under development, or if the C:N ratio
509 becomes higher than physiological bounds, the filament splits to expose a region where diazotroph
510 development may begin. A photoautotroph can be placed at any open site. Since there are two ends
511 on every filament, up to two of these decisions are being made during each simulation time step.
512 After filament splitting, if the split results in a homogenous region of either diazotrophs or
513 photoautotrophs, the missing cell type is preferred. Filaments split in the middle of the longest
514 region of homogenous cells and are prevented from splitting to result in a single cell, meaning that
515 the shortest possible resulting splits are two cells in length. Cell division completes within one
516 time step when metabolites and biomass are equally divided between parent and daughter cell and
517 the filament updates to contain the cell at its end. This decision is a memoryless process conducted
518 each time step. This means that cell division is completely metabolically motivated (which is
519 affected, in turn, by diffusion and physiological processes).

520

521 **Parameter Estimation.** As described previously, to improve the accuracy of simulations, the
 522 model was fit to experimental data for cells grown in 100 μE light in YBC-II medium. Maintenance
 523 energy, in the form of the ATP hydrolysis reaction, is the main parameter that is adjusted in FBA
 524 formulations (3, 69-72) to match simulations with growth rate. Since maintenance energy at 100
 525 μE was higher than the energetic capacity of the model for growth at 50 μE , a linear correlation
 526 was interpolated from experiments at 100 μE and 80 μE with ATP maintenance flux fit to both
 527 cases for each cell type:

$$v_{ATP}(I) = mI + v_0 \quad (22)$$

528 Where m and v_0 are calculated using the point-slope equation for a linear equation:

$$m = \frac{v_{ATP,I_1} - v_{ATP,I_2}}{I_1 - I_2} \quad (23)$$

$$v_0 = -I_1 m + v_{ATP,I_1} \quad (24)$$

529 Where I_1 is 100 μE and I_2 is 80 μE . The estimated values of the linear equation are recorded below
 530 in Table 1. If the model is unable to satisfy its maintenance demand (through any metabolic
 531 process, including catabolizing its own biomass), the cell dies. L_0 is the energy required in zero
 532 light to maintain the cell without active metabolism.

533

Table 1: ATP maintenance flux requirements estimated as a function of light intensity for Pareto Fitting.

Cell Type	Maintenance Energy, v_{ATP}		m $\left(\frac{\text{mmol}}{\text{g DW h } \mu\text{E}}\right)$	v_0 $\left(\frac{\text{mmol}}{\text{g DW h}}\right)$	L_0 (μE)
	80 μE $\left(\frac{\text{mmol}}{\text{g DW h}}\right)$	100 μE $\left(\frac{\text{mmol}}{\text{g DW h}}\right)$			
Photoautotroph	34.3	53.3	0.952	-16.7	16.9
Diazotroph	62.3	82.0	0.987	-41.9	44.0

534

535 **Multi-Objective Optimization.** Unlike typical formulations of flux balance analysis (14, 71-76),
536 which use a single objective function to predict fluxes, our model uses multi-objective
537 optimization to more accurately approximate the true objectives of the cell: to optimize biomass
538 while also producing the metabolite they exchange between cell types. Implementation of multi-
539 objective optimization is more complex and computationally intense than single objective
540 optimization therefore, to minimize computational effort, Pareto Fronts were generated *a priori* by
541 iteratively increasing ATP maintenance flux and using every permutation of objective weights to
542 fit to a dominant front (see *SI Methods* and Figure S8 for more complete details). For each point
543 along the Pareto Front, Euclidean distance was used to determine the relative weight of each
544 objective function, which was then used to generate a single, scalarized reaction. Each cell in the
545 simulation calculates its scalar objective function separately during each time step based on its
546 internal constitution and requirements.

547

548 **Implementation of Mutable Objective Functions.** Previous studies have used static objective
549 functions, where production is consistent during every phase of growth. However, organisms
550 accumulate and digest metabolites during growth and development. To reflect this, we inserted a
551 “mutable” objective function where relative preferences of storage compounds and biomass
552 production can be tailored by the agent based on cell biomass. The scalarized objective equation
553 was thus broken into two main components: storage compounds (cyanophycin modeled as β -
554 aspartyl arginine and glycogen modeled as maltose) and biomass (lipids, proteins, DNA, RNA,
555 chlorophyll, phycoerythrin, etc.). We assumed that biomass remained relatively stable throughout
556 the day while the amount of storage compound was allowed to vary. The scalar weights, or

557 production priorities, were manipulated assuming cells do not grow beyond twice their average
558 cell without dividing: lower biomass prioritizes growth and higher biomass prioritizes vegetative
559 storage compound production. Mathematically, this is modeled such that the scalar objective
560 equation's biomass coefficient was inversely adjusted by cumulative probability of a cell's
561 biomass in the distribution. The normal distribution was formulated assuming cubic 10 μm cells
562 with density of water (77) as the average mass and a narrow distribution with a standard deviation
563 of 0.433 times the mean size. This value was chosen to promote switch-like bistable behavior
564 between cell phenotypes: either cells are biomass driven (exponential) or they are metabolite
565 driven with combinations of probabilities in between. This is because a single sample of a cell
566 from a distribution of cells would have a probability of 99% to fall between 0 and twice the mean
567 size. The final distribution is:

$$f(X) \sim N(1.029 \text{ ng}, 0.433 \cdot 1.029 \text{ ng}) \quad (25)$$

568 Calculation of new objective coefficients was done by first finding the cumulative probability (z)
569 of another randomly selected cell's non-metabolite biomass being less than or equal to the
570 objective cell's biomass at each time point for each cell:

$$z = F(X \leq x_i) \quad (26)$$

571 This is used to adjust the average, experimentally matched objective coefficient (\bar{w}_b) for biomass
572 by multiplying that coefficient by the probability of the cell being larger than that size, a value that
573 represents the probabilistic expansion space (ϵ) of the cell:

$$\epsilon = 1 - z \quad (27)$$

$$\hat{w}_b = \epsilon \cdot \bar{w}_b \quad (28)$$

574 Major metabolite coefficients for the scalarized objective equation were also adjusted using this
575 probability, increasing as the cell's size increased:

$$\hat{w}_m = z \cdot \bar{w}_m \quad (29)$$

576 Finally, the coefficients are normalized such that:

$$a \sum_i \hat{w}_i = 1 \quad (30)$$

577 Or:

$$a = \frac{1}{\sum_i \hat{w}_i} \quad (31)$$

578 Which yields final objective coefficients of:

$$w_k = \frac{\hat{w}_k}{\sum_i \hat{w}_i} \quad \forall k \in \mathcal{O} \quad (32)$$

579 Where \mathcal{O} is the set of all objective metabolites in the original scalar equation.

580 Performance evaluation of the mutable objective function, validation of the mutable objective
581 function versus the static version, and justification of non-metabolite biomass as the independent
582 objective are provided in *SI Methods* and Figure S9.

583

584 **ABBREVIATIONS.** 6PG: 6-phospho-D-gluconate, 6PGDL: 6-phosph-D-glucono-1,5-lactone,
585 ABM: Agent-Based Modeling, AcCoA: Acetyl-CoA, AKG/ α KG: α -ketoglutarate/2-oxoglutarate,
586 ALA: L-alanine, β ASP-ARG, β -aspartyl arginine, β G6P: β -glucose-6-phosphate, CBB: Calvin-
587 Benson-Bassham Cycle, CDeg: Cyanophycin Degradation to Amino Acids, cEFMA: community
588 Elementary Flux Mode Analysis, CIT: Citrate, COBRA: Constraint-Based Reconstruction and
589 Analysis Toolbox, CobraPy: Constraint-Based Reconstruction and Analysis Toolbox for Python,
590 COMETS: Computation of Microbial Ecosystems in Time and Space, CSV, Comma Separated

591 Value, cph: Cyanophycin, CSyn: Cyanophycin Synthesis from Amino Acids, dFBA: dynamic Flux
592 Balance Analysis, DHAP: Dihydroxyacetone phosphate, DON: Dissolved Organic Nitrogen,
593 E4P: Erythrose-4-phosphate, EF: Efflux, EX: Export, F6P: Fructose-6-phosphate, FBA: Flux
594 Balance Analysis, FDP: Fructose 1,6-diphosphate, FOR: Formate, FUM: Fumarate, FVA: Flux
595 Variability Analysis, G6P: Glucose-6-phosphate, GAP: Glyceraldehyde 3-phosphate, GDeg:
596 Glycogen degradation, GLX: Glyoxylate (flux maps) or Glyoxylate and dicarboxylate metabolism
597 (Figure 4), GLY: Glycine (flux maps) or Glycogen/Gluconeogenesis (Figure 4), gly: Glycogen,
598 GLYR: Glycerate, GOL: Glycerol, GP: 3-phosphoglycerate, GSyn: Glycogen synthesis,
599 ICIT: Isocitrate, IN: Influx, JSON: JavaScript Object Notation, jyCOBRA: java-python integrated
600 COBRA, KEGG: Kyoto Encyclopedia of Genes and Genomes, LIP: Lipid metabolism,
601 MAL: Malate, MSM: Multiscale Modeling, OAA: Oxaloacetate, PEP: Phosphoenolpyruvate,
602 PGOL: Phosphoglycolate, Pi: Inorganic phosphate, PPP: Oxidative Pentose Phosphate Pathway,
603 PRO: Protein synthesis, PYR: Pyruvate, R5P: Ribose-5-phosphate, REF: Reflux, Ru5P: Ribulose-
604 5-phosphate, RuBP: Ribulose 1,5-bisphosphate, S17P: Sedoheptulose 1,7-bisphosphate,
605 S7P: Sedoheptulose 7-phosphate, SBML: Systems Biology Markup Language, SUCC: Succinate,

606 SUCSAL: Succinic semialdehyde, SDA: Subsystem Distribution Analysis, TCA: Tricarboxylic
607 acid cycle, TCP/IP: Transmission Control Protocol/Internet Protocol, X5P: Xylulose 5-phosphate

608 **DECLARATIONS**

609 *Competing Interests*

610 The authors declare that they have no competing interests.

611 *Funding*

612 This work was supported by a grant from the Department of Energy Office of Science, Biological
613 and Environmental Research (BER) Early Career Program grant no. DE-SC0019171.

614 *Availability of data and materials*

615 The ABM framework and datasets resulting/analyzed from simulations are available on the
616 GitHub repository at <https://github.com/boylelab/iTery101-ABM> with username “boylelab” and
617 password “diaz01”. We will make this public upon publication.

618 *Author contributions*

619 JJG, BMSH and NRB designed the research. JJG performed the research. JJG and NRB analyzed
620 the data. JJG, BMSH and NRB wrote the manuscript.

621 *Acknowledgements*

622 Not applicable.

623

624 **REFERENCES**

- 625 1. Boatman TG, Lawson T, Geider RJ. A key marine diazotroph in a changing ocean: The
626 interacting effects of temperature, CO₂ and light on the growth of *Trichodesmium erythraeum*
627 IMS101. *PloS one*. 2017;12(1):e0168796.
- 628 2. Breitbarth E, Wohlers J, Kläs J, LaRoche J, Peeken I. Nitrogen fixation and growth rates
629 of *Trichodesmium* IMS-101 as a function of light intensity. *Marine Ecology Progress Series*.
630 2008;359:25-36.
- 631 3. Gardner JJ, Boyle NR. The use of genome-scale metabolic network reconstruction to
632 predict fluxes and equilibrium composition of N-fixing versus C-fixing cells in a diazotrophic
633 cyanobacterium, *Trichodesmium erythraeum*. *BMC systems biology*. 2017;11(1):4.
- 634 4. Blazeck J, Alper H. Systems metabolic engineering: Genome-scale models and beyond.
635 *Biotechnology Journal*. 2010;5(7):647-59.
- 636 5. Tenazinha N, Vinga S. A Survey on Methods for Modeling and Analyzing Integrated
637 Biological Networks. *Computational Biology and Bioinformatics, IEEE/ACM Transactions on*.
638 2011;8(4):943-58.
- 639 6. Kranz SA, Dieter S, Richter K-U, Rost B. Carbon acquisition by *Trichodesmium*: the effect
640 of pCO₂ and diurnal changes. *Limnology and Oceanography*. 2009;54(2):548-59.
- 641 7. Flynn KJ. Ecological modelling in a sea of variable stoichiometry: dysfunctionality and the
642 legacy of Redfield and Monod. *Progress in Oceanography*. 2010;84(1-2):52-65.
- 643 8. Mahadevan R, Schilling C. The effects of alternate optimal solutions in constraint-based
644 genome-scale metabolic models. *Metabolic engineering*. 2003;5(4):264-76.
- 645 9. Hutchins D, Fu F-X, Zhang Y, Warner M, Feng Y, Portune K, et al. CO₂ control of
646 *Trichodesmium* N₂ fixation, photosynthesis, growth rates, and elemental ratios: Implications for
647 past, present, and future ocean biogeochemistry. *Limnology and Oceanography*. 2007;52(4):1293-
648 304.
- 649 10. Spungin D, Berman-Frank I, Levitan O. *Trichodesmium*'s strategies to alleviate
650 phosphorus limitation in the future acidified oceans. *Environmental microbiology*.
651 2014;16(6):1935-47.
- 652 11. Covert MW, Schilling CH, Famili I, Edwards JS, Goryanin II, Selkov E, et al. Metabolic
653 modeling of microbial strains in silico. *Trends Biochem Sci*. 2001;26.
- 654 12. Karr JR, Sanghvi JC, Macklin DN, Gutschow MV, Jacobs JM, Bolival Jr B, et al. A whole-
655 cell computational model predicts phenotype from genotype. *Cell*. 2012;150(2):389-401.
- 656 13. Harcombe WR, Riehl WJ, Dukovski I, Granger BR, Betts A, Lang AH, et al. Metabolic
657 resource allocation in individual microbes determines ecosystem interactions and spatial
658 dynamics. *Cell reports*. 2014;7(4):1104-15.
- 659 14. Mahadevan R, Edwards JS, Doyle FJ. Dynamic flux balance analysis of diauxic growth in
660 *Escherichia coli*. *Biophysical journal*. 2002;83(3):1331-40.
- 661 15. Zhuang K, Ma E, Lovley DR, Mahadevan R. The design of long-term effective uranium
662 bioremediation strategy using a community metabolic model. *Biotechnology and bioengineering*.
663 2012;109(10):2475-83.
- 664 16. Zomorodi AR, Maranas CD. OptCom: a multi-level optimization framework for the
665 metabolic modeling and analysis of microbial communities. *PLoS Comput Biol*.
666 2012;8(2):e1002363.
- 667 17. Zomorodi AR, Islam MM, Maranas CD. d-OptCom: dynamic multi-level and multi-
668 objective metabolic modeling of microbial communities. *ACS synthetic biology*. 2014;3(4):247-
669 57.

- 670 18. Oberhardt MA, Zarecki R, Gronow S, Lang E, Klenk H-P, Gophna U, et al. Harnessing the
671 landscape of microbial culture media to predict new organism–media pairings. *Nature*
672 *communications*. 2015;6:8493.
- 673 19. Oberhardt M, Palsson B, Papin J. Applications of genome-scale metabolic reconstructions.
674 *Mol Syst Biol*. 2009;5:320.
- 675 20. Fiegna F, Moreno-Letelier A, Bell T, Barraclough TG. Evolution of species interactions
676 determines microbial community productivity in new environments. *The ISME journal*.
677 2015;9(5):1235.
- 678 21. Borshchev A, Filippov A, editors. From system dynamics and discrete event to practical
679 agent based modeling: reasons, techniques, tools. Proceedings of the 22nd international conference
680 of the system dynamics society; 2004: Citeseer.
- 681 22. Klann M, Lapin A, Reuss M. Agent-based simulation of reactions in the crowded and
682 structured intracellular environment: Influence of mobility and location of the reactants. *BMC*
683 *Systems Biology*. 2011;5(1):71.
- 684 23. Segovia-Juarez JL, Ganguli S, Kirschner D. Identifying control mechanisms of granuloma
685 formation during *M. tuberculosis* infection using an agent-based model. *Journal of Theoretical*
686 *Biology*. 2004;231(3):357-76.
- 687 24. Parunak HVD. Practical and industrial applications of agent-based systems. Environmental
688 Research Institute of Michigan (ERIM). 1998.
- 689 25. Bin C, Gang G, Xiaogang Q, editors. The Application of Multi-paradigm Modeling in
690 Social Computation. Digital Manufacturing and Automation (ICDMA), 2013 Fourth International
691 Conference on; 2013 29-30 June 2013.
- 692 26. Hardebolle C, Boulanger F. Exploring Multi-Paradigm Modeling Techniques.
693 *SIMULATION*. 2009;85(11-12):688-708.
- 694 27. Hodge B-M, Shukla A, Huang S, Reklaitis G, Venkatasubramanian V, Pekny J. Multi-
695 Paradigm Modeling of the Effects of PHEV Adoption on Electric Utility Usage Levels and
696 Emissions. *Industrial & Engineering Chemistry Research*. 2011;50(9):5191-203.
- 697 28. Hodge B-MS, Huang S, Sirola JD, Pekny JF, Reklaitis GV. A multi-paradigm modeling
698 framework for energy systems simulation and analysis. *Computers & Chemical Engineering*.
699 2011;35(9):1725-37.
- 700 29. Mosterman PJ, Vangheluwe H. Computer Automated Multi-Paradigm Modeling: An
701 Introduction. *SIMULATION*. 2004;80(9):433-50.
- 702 30. Machado D, Costa R, Rocha M, Ferreira E, Tidor B, Rocha I. Modeling Formalisms in
703 *Systems Biology*. *AMB Express*. 2011;1(1):45.
- 704 31. Simons M, Misra A, Sriram G. Genome-Scale Models of Plant Metabolism. In: Sriram G,
705 editor. *Plant Metabolism. Methods in Molecular Biology*. 1083: Humana Press; 2014. p. 213-30.
- 706 32. Heinken A, Sahoo S, Fleming RM, Thiele I. Systems-level characterization of a host-
707 microbe metabolic symbiosis in the mammalian gut. *Gut microbes*. 2013;4(1):28-40.
- 708 33. Libourel IGL, Shachar-Hill Y. Metabolic Flux Analysis in Plants: From Intelligent Design
709 to Rational Engineering. *Annual Review of Plant Biology*. 2008;59(1):625-50.
- 710 34. Mahadevan R, Edwards JS, Doyle Iii FJ. Dynamic Flux Balance Analysis of Diauxic
711 Growth in *Escherichia coli*. *Biophysical Journal*. 2002;83(3):1331-40.
- 712 35. Zhuang K, Ma E, Lovley DR, Mahadevan R. The design of long-term effective uranium
713 bioremediation strategy using a community metabolic model. *Biotechnol Bioeng*. 2012;109.
- 714 36. Berman-Frank I, Lundgren P, Falkowski P. Nitrogen fixation and photosynthetic oxygen
715 evolution in cyanobacteria. *Research in Microbiology*. 2003;154:157-64.

- 716 37. Glibert PM, Bronk DA. Release of Dissolved Organic Nitrogen by Marine Diazotrophic
717 Cyanobacteria, *Trichodesmium* spp. Applied and Environmental Microbiology.
718 1994;60(11):3996-4000.
- 719 38. Burnat M, Herrero A, Flores E. Compartmentalized cyanophycin metabolism in the
720 diazotrophic filaments of a heterocyst-forming cyanobacterium. Proceedings of the National
721 Academy of Sciences. 2014;111(10):3823-8.
- 722 39. Sherman DM, Tucker D, Sherman LA. Heterocyst development and localization of
723 cyanophycin in N₂-fixing cultures of *Anabaena* sp. PCC 7120 (cyanobacteria). Journal of
724 Phycology. 2000;36(5):932-41.
- 725 40. Simon RD. Cyanophycin granules from the blue-green alga *Anabaena cylindrica*: a reserve
726 material consisting of copolymers of aspartic acid and arginine. Proceedings of the national
727 academy of sciences. 1971;68(2):265-7.
- 728 41. Levitan O, Brown CM, Sudhaus S, Campbell D, LaRoche J, Berman-Frank I. Regulation
729 of nitrogen metabolism in the marine diazotroph *Trichodesmium* IMS101 under varying
730 temperatures and atmospheric CO₂ concentrations. Environmental microbiology.
731 2010;12(7):1899-912.
- 732 42. Eichner M, Thoms S, Kranz SA, Rost B. Cellular inorganic carbon fluxes in
733 *Trichodesmium*: a combined approach using measurements and modelling. Journal of
734 experimental botany. 2014;66(3):749-59.
- 735 43. Buitenhuis E, Vogt M, Moriarty R, Bednarsek N, Doney S, Leblanc K, et al. MAREDAT:
736 towards a world atlas of MARine Ecosystem DATa. Earth System Science Data. 2013;5:227-39.
- 737 44. Berman-Frank I, Lundgren P, Chen Y-B, Küpper H, Kolber Z, Bergman B, et al.
738 Segregation of Nitrogen Fixation and Oxygenic Photosynthesis in the Marine Cyanobacterium
739 *Trichodesmium*. Science. 2001;294(5546):1534-7.
- 740 45. Zhang S, Bryant DA. The Tricarboxylic Acid Cycle in Cyanobacteria. Science.
741 2011;334(6062):1551-3.
- 742 46. Luo Y, Doney S, Anderson L, Benavides M, Berman-Frank I, Bode A, et al. Database of
743 Diazotrophs in Global Ocean: Abundance, Biomass, and Nitrogen Fixation Rates. Earth System
744 Science Data. 2012;4(1).
- 745 47. White AE, Watkins-Brandt KS, Church MJ. Temporal Variability of *Trichodesmium* spp.
746 and Diatom-Diazotroph Assemblages in the North Pacific Subtropical Gyre. Frontiers in Marine
747 Science. 2018;5:27.
- 748 48. Yoo S-H, Keppel C, Spalding M, Jane J-l. Effects of growth condition on the structure of
749 glycogen produced in cyanobacterium *Synechocystis* sp. PCC6803. International journal of
750 biological macromolecules. 2007;40(5):498-504.
- 751 49. Cai X, Gao K, Fu F, Campbell DA, Beardall J, Hutchins DA. Electron transport kinetics in
752 the diazotrophic cyanobacterium *Trichodesmium* spp. grown across a range of light levels.
753 Photosynthesis research. 2015;124(1):45-56.
- 754 50. Schuetz R, Kuepfer L, Sauer U. Systematic evaluation of objective functions for predicting
755 intracellular fluxes in *Escherichia coli*. Mol Syst Biol. 2007;3:119.
- 756 51. Blaby IK, Glaesener AG, Mettler T, Fitz-Gibbon ST, Gallaher SD, Liu B, et al. Systems-
757 Level Analysis of Nitrogen Starvation-Induced Modifications of Carbon Metabolism in a
758 *Chlamydomonas reinhardtii* Starchless Mutant. The Plant Cell Online. 2013;25(11):4305-23.
- 759 52. Boyle NR, Page MD, Liu B, Blaby IK, Casero D, Kropat J, et al. Three Acyltransferases
760 and Nitrogen-responsive Regulator Are Implicated in Nitrogen Starvation-induced Triacylglycerol
761 Accumulation in *Chlamydomonas*. Journal of Biological Chemistry. 2012;287(19):15811-25.

- 762 53. Breuer G, Lamers PP, Martens DE, Draaisma RB, Wijffels RH. The impact of nitrogen
763 starvation on the dynamics of triacylglycerol accumulation in nine microalgae strains. *Bioresource*
764 *Technology*. 2012;124:217-26.
- 765 54. Hockin NL, Mock T, Mulholland F, Kopriva S, Malin G. The Response of Diatom Central
766 Carbon Metabolism to Nitrogen Starvation Is Different from That of Green Algae and Higher
767 Plants. *Plant Physiology*. 2012;158(1):299-312.
- 768 55. Tedesco MA, Duerr EO. Light, temperature and nitrogen starvation effects on the total
769 lipid and fatty acid content and composition of *Spirulina platensis* UTEX 1928. *Journal of Applied*
770 *Phycology*. 1989;1(3):201-9.
- 771 56. Kropat J, Hong-Hermesdorf A, Casero D, Ent P, Castruita M, Pellegrini M, et al. A revised
772 mineral nutrient supplement increases biomass and growth rate in *Chlamydomonas reinhardtii*.
773 *The Plant journal : for cell and molecular biology*. 2011;66(5):770-80.
- 774 57. Boatman TG, Davey PA, Lawson T, Geider RJ. The physiological cost of diazotrophy for
775 *Trichodesmium erythraeum* IMS101. *PloS one*. 2018;13(4):e0195638.
- 776 58. Boatman TG, Davey PA, Lawson T, Geider RJ. CO₂ modulation of the rates of
777 photosynthesis and light-dependent O₂ consumption in *Trichodesmium*. *Journal of experimental*
778 *botany*. 2018;70(2):589-97.
- 779 59. Boatman TG, Mangan NM, Lawson T, Geider RJ. Inorganic carbon and pH dependency
780 of photosynthetic rates in *Trichodesmium*. *Journal of experimental botany*. 2018:ery141.
- 781 60. Chen Y-B, Zehr JP, Mellon M. Growth and Nitrogen Fixation of the Diazotrophic
782 Filamentous Nonheterocytous Cyanobacterium *Trichodesmium* sp. IMS 101 in Defined Media:
783 Evidence for a Circadian Rhythm. *Journal of Phycology*. 1996;32(6):916-23.
- 784 61. Harris EH, Stern DB, Witman G. *The Chlamydomonas sourcebook*: Cambridge Univ
785 Press; 2009.
- 786 62. Yemm E, Willis A. The estimation of carbohydrates in plant extracts by anthrone.
787 *Biochemical journal*. 1954;57(3):508.
- 788 63. Messineo L. Modification of the Sakaguchi reaction: spectrophotometric determination of
789 arginine in proteins without previous hydrolysis. *Archives of Biochemistry and Biophysics*.
790 1966;117(3):534-40.
- 791 64. Liddicoat M, Tibhitts S, Butler E. The determination of ammonia in seawater. *Limnology*
792 *and Oceanography*. 1975;20(1):131-2.
- 793 65. Collier N, North M. Parallel agent-based simulation with repast for high performance
794 computing. *Simulation*. 2013;89(10):1215-35.
- 795 66. Grajdeanu A. Modeling Diffusion in a Discrete Environment. George Mason University
796 Technical Report Series. 2007:1-5.
- 797 67. Sandh G, Ran L, Xu L, Sundqvist G, Bulone V, Bergman B. Comparative proteomic
798 profiles of the marine cyanobacterium *Trichodesmium erythraeum* IMS101 under different
799 nitrogen regimes. *Proteomics*. 2011;11(3):406-19.
- 800 68. Pfreundt U, Kopf M, Belkin N, Berman-Frank I, Hess WR. The primary transcriptome of
801 the marine diazotroph *Trichodesmium erythraeum* IMS101. *Scientific reports*. 2014;4.
- 802 69. Boyle NR, Shastri AA, Morgan JA. Network Stoichiometry In: Schwender J, editor. *Plant*
803 *Metabolic Networks*. New York: Springer New York 2009. p. 211-43.
- 804 70. Boyle N, Morgan J. Flux balance analysis of primary metabolism in *Chlamydomonas*
805 *reinhardtii*. *BMC Systems Biology*. 2009;3(1):4.

- 806 71. Knoop H, Gründel M, Zilliges Y, Lehmann R, Hoffmann S, Lockau W, et al. Flux Balance
807 Analysis of Cyanobacterial Metabolism: The Metabolic Network of *Synechocystis* sp. PCC 6803.
808 PLoS Comput Biol. 2013;9(6):e1003081.
- 809 72. Misra A, Conway MF, Johnnie J, Qureshi TM, Derrick AM, Agbo EC, et al. Metabolic
810 analyses elucidate nontrivial gene targets for amplifying dihydroartemisinic acid production in
811 yeast. *Frontiers in Microbiology*. 2013;4.
- 812 73. Orth JD, Thiele I, Palsson BO. What is flux balance analysis? *Nat Biotech*. 2010;28(3):245-
813 8.
- 814 74. Kauffman KJ, Prakash P, Edwards JS. Advances in flux balance analysis. *Current Opinion*
815 *in Biotechnology*. 2003;14(5):491-6.
- 816 75. Edwards J, Ramakrishna R, Schilling C, Palsson B. Metabolic flux balance analysis.
817 *Metabolic engineering*. 1999.
- 818 76. Asadollahi MA, Maury J, Patil KR, Schalk M, Clark A, Nielsen J. Enhancing sesquiterpene
819 production in *Saccharomyces cerevisiae* through in silico driven metabolic engineering. *Metabolic*
820 *Engineering*. 2009;11(6):328-34.
- 821 77. van Baalen C, Brown Jr RM. The ultrastructure of the marine blue green alga,
822 *Trichodesmium erythraeum*, with special reference to the cell wall, gas vacuoles, and cylindrical
823 bodies. *Archiv für Mikrobiologie*. 1969;69(1):79-91.

824